

Do single-shot projective readouts necessarily estimate the T_1 lifetime ?

Aparajita Modak,¹ Sundeep Kapila,¹ Bent Weber,² Klaus Ensslin,³ Guido Burkard,⁴ and Bhaskaran Muralidharan^{1,*}

¹*Department of Electrical Engineering, Indian Institute of Technology Bombay, Powai, Mumbai-400076, India*

²*Division of Physics and Applied Physics, School of Physical and Mathematical Sciences, Nanyang Technological University, Singapore 637371, Singapore*

³*Laboratory for Solid State Physics, ETH Zurich, CH-8093 Zurich, Switzerland*

⁴*Department of Physics, University of Konstanz, D-78457, Germany*

(Dated: March 12, 2026)

When single-shot qubit readout protocols are adapted for multilevel systems, theoretical T_1 lifetime calculations often fall short of capturing the experimental lifetime trends. We identify *extrinsic* population dynamics as the fundamental origin of this disparity, establishing that the lifetime estimates can, in certain operating regions, be distinct from the intrinsic T_1 time. We clarify these aspects with an integrated theory to address recent measurements [**Nat. Nano**, **20**, **494**, (2025)] on spin-valley states in bilayer graphene. While confirming that phonon and Johnson noise are the dominant intrinsic sources, we show that the inclusion of extrinsic factors provide the critical match to the experimental estimates. The extrinsic factors also effectuate violations of generalized Mathiessen's rules also. With an improved handle on the design space, a revised readout protocol to estimate the T_1 lifetime of the valley qubit is proposed.

In any physical realization of quantum computation [1], the T_1 lifetime of a qubit is a critical performance parameter as it asserts the immunity to environmental noise. It is defined as the longitudinal relaxation time of a quantum two-state system (QTS, qubit) as a result of *intrinsic* ambient noise [1–3]. In the Markovian case, it limits the dephasing time T_2 , with $T_2 \leq 2T_1$ [4].

In semiconductor quantum dots [5–7], the T_1 time is estimated by employing the single-shot projective readout, also called the Elzerman readout technique [8–10]. The implementation [10] on a QTS such as a Zeeman spin qubit [8] yields an accurate estimate of the spin- T_1 time. The presence of closely placed excited states (ES) near the probed states of interest, degeneracies and level anticrossings, however, are inevitable in semiconductor systems of current interest, such as Si, 2D-material platforms like bilayer graphene (BLG) and transition metal dichalcogenides [8, 11–18], due to the coupling of spins and inequivalent valleys.

The ERT can be adapted for the multilevel case also [19] via energy selective *readout protocols* [10] that probe the two states of interest as schematized in Fig. 6(a). The load and read cycles are facilitated by single charge tunneling events involving a fermionic reservoir. For a viable T_1 estimate, the energy separation must hence be sufficiently larger than the thermal energy. Despite satisfying the aforesaid criterion, we establish here that the effective lifetimes obtained from a multilevel energy selective ERT [11, 19] can be distinct from the T_1 time.

Recent measurements [11] on bilayer graphene quantum dots (BLG-QDs) provide the requisite backdrop while simultaneously facilitating a testbed for a necessary theory-experiment synergy. Figure 6(b) shows a schematic of the energy landscape of a singly occupied BLG-QD with an applied out-of-plane magnetic field B_\perp .

This platform can host the spin, valley and the spin-valley (Kramers) qubit, whose operating points can be tuned as B_\perp is varied. Among these, the Kramers qubit promises ultra-long T_1 times [11, 20], owing to the need for a simultaneous flip of the spin and the valley state near zero magnetic fields; due to what is known as the van Vleck cancellation [21].

To distinguish the T_1 time from an effective lifetime, especially around degeneracies and anticrossings, one has to disentangle the intrinsic decay pathways from the *extrinsic* ones that include stochastic loading, hybridization, and the proximity to nearby ES. The intrinsic point of view that defines the T_1 time is schematized in Fig. 6(c), while the extrinsic factors that alter the population dynamics are depicted via the state transition diagram in Fig. 6(d). To faithfully reproduce the experimentally estimated lifetimes, as shown in Fig. 7, we develop a two-tier approach, that blends in the extrinsic factors. We integrate the extrinsic dynamics described by the master equation (ME) formulation [5, 22, 23] over the intrinsic noise models evaluated using the Fermi's golden rule (FGR) approach [7, 24–28].

Our intrinsic calculations indeed ratify the experimentally measured ultralong Kramers T_1 times and that the phonon and Johnson noise are the dominant sources of noise. However, Fig. 7 also points out that the intrinsic treatment alone underestimates the relaxation rate specifically in the B_\perp range of the shaded regions. As an extreme case marked in Fig. 7, the experiment reports a Kramers lifetime approximately 4 s longer than the intrinsic T_1 at $B_\perp = 0.075$ T, which is around the valley anti-crossing region.

Cementing the role of both intrinsic and extrinsic contributions, we refer back to the theory-experiment agreement in Fig. 7, where the experimentally measured qubit lifetimes ($T_{1,m}$) and the associated measurement protocols (inset) are shown. The blue and green data points partially follow intrinsic trends, whereas the black data

* Corresponding author: bm@ee.iitb.ac.in

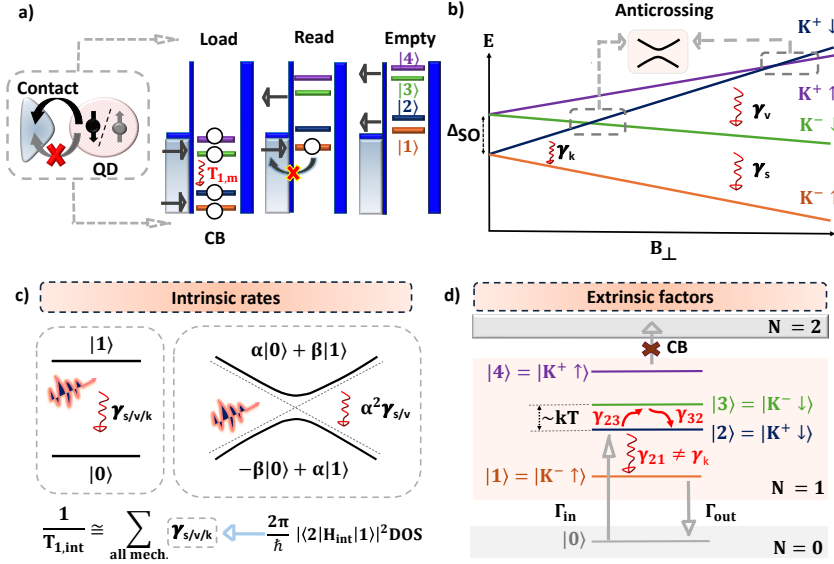


FIGURE 1. Preliminaries. (a) ERT based on energy-selective tunneling between the dot and the reservoir. (b) Representative energy spectrum of the four spin–valley states as a function of B_{\perp} . The first anticrossing occurs when E_Z equals Δ_{SO} , with t_v inducing hybridized eigenstates. A second, weaker anticrossing appears at higher fields due to intravalley mixing, leading to a modified state composition. The intrinsic relaxation channels, spin (γ_s), valley (γ_v), and Kramers (γ_k) are indicated. (c) Intrinsic pathway away from, and near the anticrossing, which involves state–mixing. (d) Extrinsic factors: population dynamics which modify the experimentally inferred lifetime.

points follow a combination of γ_s and γ_v , the valley and spin relaxation rates respectively. The shaded regions around the anticrossing require the inclusion of extrinsic analysis. The additional pathways activated by these contributions also lead to a violation of the generalized Matthiessen’s harmonic sum rule of the individual lifetimes.

Preliminaries. Neglecting the Rashba spin-orbit coupling [29, 30], the effective Hamiltonian of the BLG-QD in a homogeneous B_{\perp} is,

$$\begin{aligned} \hat{H}_{QD} = & \epsilon_0 \hat{n} + t_v \sum_{\sigma} \left(\hat{c}_{K^+\sigma}^{\dagger} \hat{c}_{K^-\sigma} + \text{h.c.} \right) \\ & + \frac{1}{2} \sum_{\tau, \sigma} \hat{c}_{\tau\sigma}^{\dagger} \left[\Delta_{\text{SO}} \tau_z s_z + \mu_B B_{\perp} (g_s s_z + g_v \tau_z) \right] \hat{c}_{\tau\sigma} \\ & + \frac{U}{2} (\hat{n}^2 - \hat{n}). \end{aligned} \quad (1)$$

where ϵ_0 is the on-site energy, $\hat{c}_{\tau\sigma}^{\dagger}$ ($\hat{c}_{\tau\sigma}$) is the creation (annihilation) operator of an electron with spin σ residing in a valley $\tau = K^{\pm}$. The term U is the single-electron charging energy, \hat{n} is the total number operator, Δ_{SO} , the intrinsic Ising SOC, $g_{s(v)}$, the spin (valley) g -factor and t_v is the intervalley mixing parameter. The Ising SOC term $\Delta_{\text{SO}} \tau_z s_z$ preserves both spin and valley quantum numbers, while the valley Zeeman coupling $\propto g_v B_{\perp} \tau_z$ shifts K^+ and K^- states oppositely. We now define the generalized Zeeman energy $E_Z = \mu_B B_{\perp} (g_s s_z + g_v \tau_z)$, which combines the spin and valley Zeeman effects.

To make the role of state mixing (hybridization) ex-

PLICIT, we begin with the spin–valley product states, $|1\rangle = |K^- \uparrow\rangle$, $|2\rangle = |K^+ \downarrow\rangle$, $|3\rangle = |K^- \downarrow\rangle$, $|4\rangle = |K^+ \uparrow\rangle$. Intervalley mixing t_v them as

$$\begin{aligned} |1\rangle &= |K^- \uparrow\rangle, \\ |\bar{2}\rangle &= \sin\left(\frac{\theta}{2}\right) |K^+ \downarrow\rangle - \cos\left(\frac{\theta}{2}\right) |K^- \downarrow\rangle, \\ |\bar{3}\rangle &= \cos\left(\frac{\theta}{2}\right) |K^+ \downarrow\rangle + \sin\left(\frac{\theta}{2}\right) |K^- \downarrow\rangle, \\ |4\rangle &= |K^+ \uparrow\rangle. \end{aligned} \quad (2)$$

Here, θ is the mixing angle determined by the interplay of Δ_{SO} , the magnetic field-induced Zeeman energy E_Z , and t_v . Perturbation theory yields $\cos^2\left(\frac{\theta}{2}\right) = \frac{\sqrt{(\Delta_{\text{SO}} - E_Z)^2 + 4t_v^2} - (\Delta_{\text{SO}} - E_Z)}{2\sqrt{(\Delta_{\text{SO}} - E_Z)^2 + 4t_v^2}}$. At the anticrossing, $\Delta_{\text{SO}} = E_Z$, and the level repulsion is determined by t_v .

Intrinsic lifetimes. The spin, valley, and Kramers qubits in BLG quantum dots are subject to several electronic noise sources, most notably, phonon noise, Johnson noise, and $1/f$ charge noise [31–34]. At GHz frequencies of relevance here, phonon and Johnson noise dominate the relaxation dynamics. In a centrosymmetric crystal like BLG [35, 36], the electron–phonon coupling (EPC) arises primarily from the deformation-potential (DP) and bond-length-change (BLC) mechanisms. We include contributions due to both longitudinal acoustic (LA) and transverse acoustic (TA) phonon branches. The in-plane EPC is described by the Hamil-

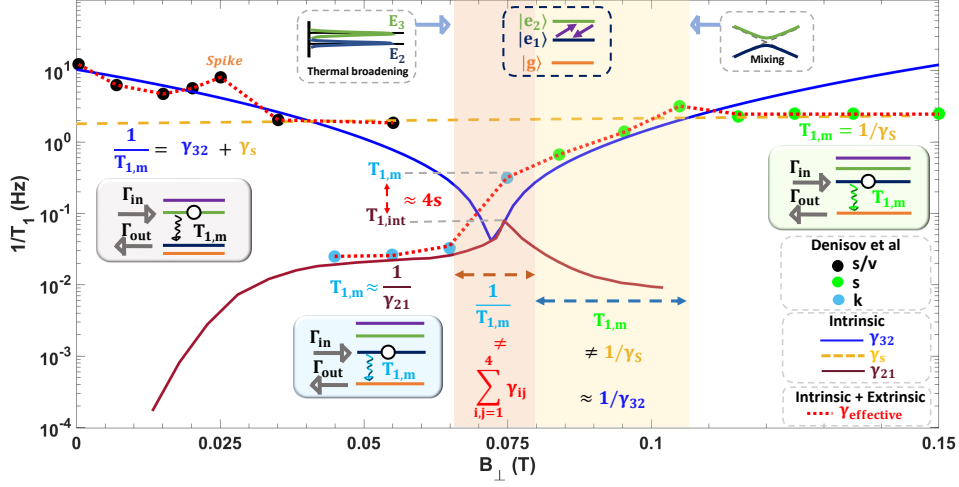


FIGURE 2. Experimental match, intrinsic and extrinsic factors. The dependence of intrinsic spin, valley and Kramers lifetimes on B_{\perp} with contributions from phonon and Johnson noise in the presence of t_v . The experimentally measured lifetimes (T_{1m}) and the corresponding readout protocols (inset). Shaded regions mark the regions where t_v and thermal broadening become relevant. The effective lifetimes ($\gamma_{\text{effective}}^{-1}$) obtained from the integrated framework capture the observed behavior. Parameters used are $g_1 = 50$ eV and $g_2 = 3$ eV (s, k), $g_1 = 50$ eV and $g_2 = 2.8$ eV (v), $J_s = 1.8$ Hz, $J_v = 2.5$ Hz, $J_k = 0.02$ Hz, $R = 30$ nm, $U_0 = 40$ meV, $\Delta_{\text{SO}} = 64$ μeV , $t_v = 1$ μeV , and $g_v = 14.5$ [11].

tonian [26, 37]

$$\hat{H}_{\text{EPC}} = K \begin{pmatrix} g_1 a_1 & g_2 a_2^* \\ g_2 a_2 & g_1 a_1 \end{pmatrix} \left(e^{i\mathbf{q}\cdot\mathbf{r}} \hat{b}_{mq}^{\dagger} - e^{-i\mathbf{q}\cdot\mathbf{r}} \hat{b}_{mq} \right), \quad (3)$$

where $K = \frac{q}{\sqrt{A\rho\omega_{qm}}}$, A is the area, ρ is the mass density, $\omega_{\mathbf{q},m}$ is the phonon frequency for the wave vector \mathbf{q} and the branch m , $g_{1(2)}$ is the coupling constant of DP(BLC), $a_{1(2)}$ are the sublattice amplitudes and \hat{b}_{mq}^{\dagger} (\hat{b}_{mq}) is the phonon creation (annihilation) operator.

In hBN-encapsulated BLG, coupling to out-of-plane flexural (ZA) phonon modes is strongly suppressed by mechanical clamping, leaving in-plane acoustic phonons as the dominant relaxation channel. Applying the FGR, the intrinsic phonon-assisted transition rates are obtained as follows (see Supplementary Note I):

$$\gamma_{\alpha}(\omega) = \sum_{m=\text{LA,TA}} \gamma_{m\alpha}^{\text{ph}}(\omega) \left(\frac{\omega}{\omega_{\text{SO}}} \right)^{n_{\alpha}} + J_{\alpha} \gamma_{\alpha}^{\text{J}}(\omega), \quad (4)$$

where $\alpha \in \{s, v, k\}$, with $n_v = 4$, $n_k = 6$, and $n_s = 2$ (DP, LA) or $n_s = 4$ (BLC, LA, TA). The spin-orbit splitting frequency is denoted by ω_{SO} . The matrix elements $\gamma_{\alpha m}^{\text{ph}}(\omega)$ arise from in-plane acoustic modes, vary only weakly with B_{\perp} at low fields and are set primarily by the dot size and sound velocities. In contrast, $\gamma_{\alpha}^{\text{J}}(\omega)$ describes the relaxation driven by Johnson noise, and J_{α} encodes the device-specific electromagnetic coupling parameters.

For small B_{\perp} , t_v is the dominant source of hybridization, and the transition rates for the four states can be

written as (see Supplementary Note II):

$$\begin{aligned} \gamma_{\bar{2}1} &= \gamma_s \cos^2\left(\frac{\theta}{2}\right) + \gamma_k \sin^2\left(\frac{\theta}{2}\right), \\ \gamma_{\bar{3}1} &= \gamma_s \sin^2\left(\frac{\theta}{2}\right) + \gamma_k \cos^2\left(\frac{\theta}{2}\right), \\ \gamma_{\bar{3}\bar{2}} &= \gamma_v \cos^2 \theta, \\ \gamma_{4\bar{3}} &= \gamma_s \cos^2\left(\frac{\theta}{2}\right) + \gamma_k \sin^2\left(\frac{\theta}{2}\right), \\ \gamma_{4\bar{2}} &= \gamma_s \sin^2\left(\frac{\theta}{2}\right) + \gamma_k \cos^2\left(\frac{\theta}{2}\right), \\ \gamma_{41} &= \gamma_v. \end{aligned} \quad (5)$$

Here, $\bar{2}$ and $\bar{3}$ denote the excited hybridized states near the anticrossing. The above illustrates that state-mixing modulates the relaxation rates γ_{α} near the anticrossing [19, 24, 38, 39]. In Fig. 7, we hence note that a finite t_v produces a dip in γ_v , whereas γ_s remains essentially constant in this regime, as the spin splitting ΔE_s varies only weakly with B_{\perp} . However, γ_v exhibits a scaling of B_{\perp}^6 . This trend is altered near the anticrossing, where t_v modifies the relaxation matrix elements as noted in the above expressions.

Extrinsic contributions. The ME framework captures the nonequilibrium populations in the eigenstate basis. Coherences between eigenstates can be neglected because they decay much faster than the intrinsic relaxation processes driven by noise and charge tunneling. A quantum master-equation treatment is, however, required when a transverse electromagnetic field is applied [40–44].

To account for the load and read operations involving the contacts, the total Hamiltonian $\hat{H} = \hat{H}_{\text{QD}} + \hat{H}_{\text{C}} + \hat{H}_{\text{T}}$, where \hat{H}_{C} and \hat{H}_{T} are the contact and tunneling Hamiltonian respectively, is considered. Here, \hat{H}_{T} is treated perturbatively [40–44] up to second order to obtain the ME for the evolution of the diagonal elements (state

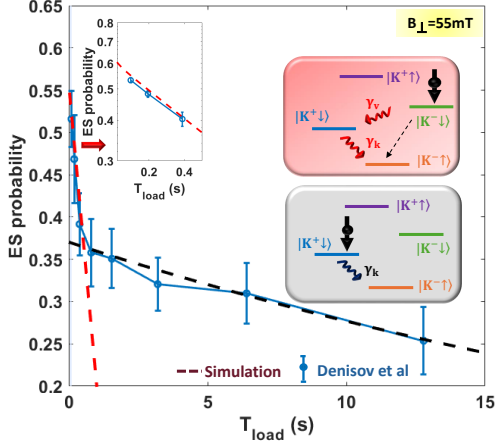


FIGURE 3. Extrinsic effects. Bi-exponential distribution of the ES probability versus T_{load} at $B_{\perp} = 55$ mT. Charge jumps occasionally load the electron into the excited state $|K^{-}\downarrow\rangle$ (top), producing fast valley-mediated relaxation. In the absence of such jumps, the system relaxes through the Kramers channel $|K^{+}\downarrow\rangle$ (bottom).

probabilities) in the BLG-QD subspace.

The BLG-QD subspace is described using a five state Fock space comprising four one-electron ($N = 1$) states and one unoccupied ($N = 0$) state. The tunnel coupling induces transitions between $N = 0$ and $N = 1$ space (Fig. 6(d)), as a part of the load and read processes. Intrinsic transitions are described by $R_{ij} = \gamma_{ij}$, while tunneling to and from the contact is given by $R_{ij} = \Gamma_{ij}$. The occupations P_i evolve according to

$$\frac{dP_i}{dt} = - \sum_j R_{ij} P_i + \sum_j R_{ji} P_j, \quad (6)$$

with $i, j = 0, 1, 2(\bar{2}), 3(\bar{3}), 4$ and $\sum_i P_i = 1$. Here, $i(j) = 0$ labels the $N = 0$ state. The dot-lead tunneling is accounted for using $\Gamma_i = \gamma_b f_i$, where $f_i = [1 + \exp((E_i - \mu_F)/k_B T_e)]^{-1}$, γ_b is the bare tunneling rate, μ_F is the electrochemical potential of the contact [22], and T_e is the electron temperature. The transients of the readout processes are captured with respect to the load time, T_{load} (See Supplementary Note IV).

As a first exposition on extrinsic effects, Fig. 3 explains the experimentally observed bi-exponential decay of the ES population with T_{load} . For the relevant parameters ($\gamma = 15$ Hz, $B_{\perp} = 55$ mT, and $T_e = 30$ mK), the second ES lies well outside the thermal window ($\Delta\epsilon \gg 3k_B T_e$) and cannot be accessed otherwise. In practical systems, stochastic charge fluctuations enable occasional loading into either ES with comparable probability [11].

This mechanism is incorporated in the simulations by initializing population in both $\bar{2}$ and $\bar{3}$, weighted by the probability of charge-offset events. The resulting fast initial decay (γ_v) and slow tail (γ_k) arise from the distinct decay pathways shown in the inset state-transition diagrams. Enforcing detailed balance,

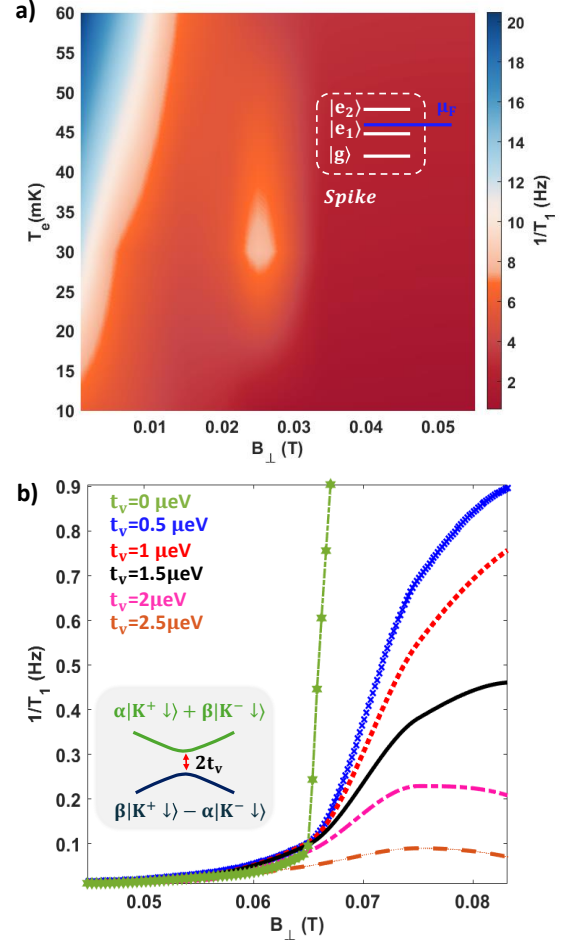


FIGURE 4. Effect of T_e and t_v on the $1/T_1$ spikes. (a) Simulated $1/T_1$ versus T_e at the spin/valley operating point where a spike is observed, which is not a typical signature. The T_e sweeps confirm a smooth increase of $1/T_1$ without any spike if the potential fluctuation is not included. (b) The $1/T_1$ versus B_{\perp} around the spin-valley anticrossing. In this region, the sharp rise in $1/T_1$ is governed by t_v . Spectral constraints result in $t_v \lesssim 2$ μeV .

$\gamma_{ji}/\gamma_{ij} = e^{-(E_j - E_i)/k_B T_e}$, the simulations reproduce both decay components, confirming that the observed scenario originates from the loading dynamics.

Consolidating the results. We observe that γ_v ($\gamma_{\bar{3}\bar{2}}$ around the anticrossing) is strongly modulated by mixing and exhibits a pronounced B_{\perp} dependence, as shown in Fig. 7. Since γ_s has a weak B_{\perp} dependence, the variations in the relaxation trends observed for the spin/valley protocol in the field range 0–55 mT are primarily due to γ_v . Accounting for multilevel dynamics, the variation of the rates observed in the 80–100 mT range (yellow patch in Fig. 7) is also dominated by valley flips.

The spike in the spin/valley data around $B_{\perp} \approx 25$ mT is reproduced by incorporating the probability of sudden dot-potential fluctuations, which transiently shift μ_F relative to the loading window [45, 46]. To substantiate this

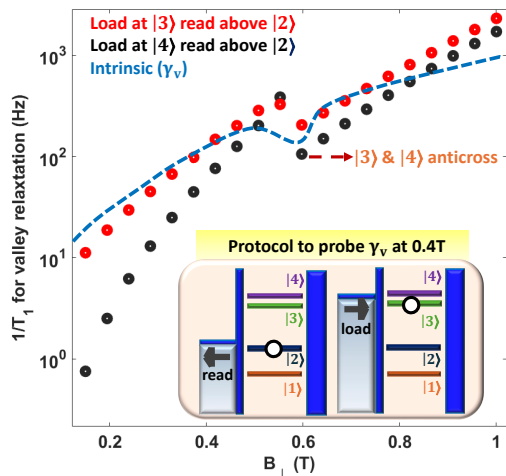


FIGURE 5. Designing readouts. Predicted valley $1/T_1$ versus B_{\perp} upto 1 T. The B_{\perp} dependence follows the γ_v with a weak non-monotonic shoulder near the second anticrossing due to t_v . The inset depicts the readout protocol.

interpretation, T_e is used as an independent control parameter. As shown in Fig. 4(a), increasing T_e uniformly degrades T_1 while preserving the B_{\perp} dependence, thereby ruling out thermal activation as the origin of the spike.

In the intermediate field range 55–78 mT (red patch in Fig. 7), variations in γ_{21} become most pronounced, reflecting the modulation of γ_k . Despite its small magnitude, t_v plays a decisive role in shaping the relaxation trend, as demonstrated in Fig. 4(b). Importantly, the mismatch in the Kramers lifetime estimate highlighted in Fig. 7 (approximately 4 s) cannot be attributed solely to the variations in t_v or to the linear combinations of γ_{32} , γ_s , and γ_{21} . The effective rate $\gamma_{\text{effective}}$ is only reproduced via the integrated framework.

Figure 5 outlines a protocol for directly probing γ_v by suppressing spin-flip pathways. Away from the anticrossing (See Supplementary Note III), this protocol will recover the intrinsic valley T_1 time. Near the anticrossing

however, mixing between the $|\bar{3}\rangle$ and $|\bar{4}\rangle$ states modifies the accessible decay pathways, such that the experimentally extracted lifetime can no longer be directly related to the intrinsic T_1 time.

Conclusion. We developed a generalized two-tier approach to provide a consistent interpretation of lifetime estimates from multilevel ERT [11] experiments. By reproducing recent experimental trends [11], we made a clear distinction between the QTS T_1 time and the effective lifetime. Near degeneracies and anticrossings, one has to resort to the effective lifetime - which is a combination of both intrinsic and extrinsic contributions. We also pointed out that the generalized Matthiessen’s rule in such cases, can also be violated. Near zero fields, one may record hours-long T_1 time if the system is tuned to probe Kramers transitions, reflecting the strong symmetry protection of Kramers pairs. The integrated approach developed here can be employed to explain many existing discrepancies between intrinsic estimates and measured lifetimes [13, 14, 20] as well as advancing further experiments in emerging qubit systems.

Acknowledgments. We acknowledge useful discussions with Lin Wang. BM acknowledges funding from the Inani Chair Professorship fund through Grant No. DO/2024-INAN/001-001, and the Department of Science and Technology, Government of India, under the National Quantum Mission through Grant no. DST/QTC/NQM/QMD/2024/4. BM and SK acknowledge funding from the Dhananjay Joshi Endowment award through Grant No: DO/2023-DJEF002. SK acknowledges the Swasth Research Fellowship. AM acknowledges the Prime Minister Research Fellowship (PMRF). BW acknowledges support from the Singapore Ministry of Education (MOE) Academic Research Fund Tier 3 grant (MOE-MOET32023-0003) “Quantum Geometric Advantage” and the Air Force Office of Scientific Research under award number FA2386-24-1-4064. GB acknowledges funding from the Deutsche Forschungsgemeinschaft (DFG, German Research Foundation) – Project No. 425217212 – SFB 1432.

-
- [1] IBM Quantum, “IBM quantum platform,” (2025).
 - [2] K. Blum, *Density matrix theory and applications*, 3rd ed., Springer series on atomic, optical, and plasma physics, Vol. 64 (Springer, Berlin, Heidelberg, 2012).
 - [3] A. Javadi-Abhari *et al.*, “Quantum computing with Qiskit,” (2024), arXiv:2405.08810 [quant-ph].
 - [4] M. A. Nielsen and I. L. Chuang, *Quantum Computation and Quantum Information: 10th Anniversary Edition* (Cambridge University Press, Cambridge, 2010).
 - [5] R. Hanson, L. P. Kouwenhoven, J. R. Petta, S. Tarucha, and L. M. K. Vandersypen, *Rev. Mod. Phys.* **79**, 1217 (2007).
 - [6] F. A. Zwanenburg, A. S. Dzurak, A. Morello, M. Y. Simmons, L. C. Hollenberg, G. Klimeck, S. Rogge, S. N. Coppersmith, and M. A. Eriksson, *Rev. Mod. Phys.* **85**, 961 (2013).
 - [7] G. Burkard, T. D. Ladd, A. Pan, J. M. Nichol, and J. R. Petta, *Rev. Mod. Phys.* **95**, 025003 (2023).
 - [8] J. Elzerman, R. Hanson, L. Willems van Beveren, B. Witkamp, L. Vandersypen, and L. P. Kouwenhoven, *Nature* **430**, 431 (2004).
 - [9] A. Morello, J. J. Pla, F. A. Zwanenburg, K. W. Chan, K. Y. Tan, H. Huebl, M. Möttönen, C. D. Nugroho, C. Yang, J. A. Van Donkelaar, *et al.*, *Nature* **467**, 687 (2010).
 - [10] R. Hanson, L. P. Kouwenhoven, J. R. Petta, S. Tarucha, and L. M. Vandersypen, *Rev. Mod. Phys.* **79**, 1217 (2007).
 - [11] A. O. Denisov, V. Reckova, S. Cances, M. J. Ruckriegel, M. Masseroni, C. Adam, C. Tong, J. D. Gerber, W. W.

- Huang, K. Watanabe, *et al.*, *Nat. Nanotechnol.* **20**, 494 (2025).
- [12] L. Banszerus, K. Hecker, S. Möller, E. Icking, K. Watanabe, T. Taniguchi, C. Volk, and C. Stampfer, *Nat. Commun.* **13**, 3637 (2022).
- [13] L. Banszerus, K. Hecker, L. Wang, S. Möller, K. Watanabe, T. Taniguchi, G. Burkard, C. Volk, and C. Stampfer, *Phys. Rev. B* **112**, 035409 (2025).
- [14] R. Garreis, C. Tong, J. Terle, M. J. Ruckriegel, J. D. Gerber, L. M. Gächter, K. Watanabe, T. Taniguchi, T. Ihn, K. Ensslin, *et al.*, *Nat. Phys.* **20**, 428 (2024).
- [15] L. M. Gächter, R. Garreis, J. D. Gerber, M. J. Ruckriegel, C. Tong, B. Kratochwil, F. K. de Vries, A. Kurzmann, K. Watanabe, T. Taniguchi, T. Ihn, K. Ensslin, and W. W. Huang, *PRX Quantum* **3**, 020343 (2022).
- [16] M. Xiao, M. House, and H. W. Jiang, *Phys. Rev. Lett.* **104**, 096801 (2010).
- [17] C. Simmons, J. Prance, B. Van Bael, T. S. Koh, Z. Shi, D. Savage, M. Lagally, R. Joynt, M. Friesen, S. Copper-smith, *et al.*, *Phys. Rev. Lett.* **106**, 156804 (2011).
- [18] L. Petit, J. Boter, H. Eenink, G. Droulers, M. Tagliaferri, R. Li, D. Franke, K. Singh, J. Clarke, R. Schouten, *et al.*, *Phys. Rev. Lett.* **121**, 076801 (2018).
- [19] C. Yang, A. Rossi, R. Ruskov, N. Lai, F. Mohiyaddin, S. Lee, C. Tahan, G. Klimeck, A. Morello, and A. Dzurak, *Nat. Commun.* **4**, 2069 (2013).
- [20] L. Banszerus, S. Möller, C. Steiner, E. Icking, S. Trelenkamp, F. Lentz, K. Watanabe, T. Taniguchi, C. Volk, and C. Stampfer, *Nat. Commun.* **12**, 5250 (2021).
- [21] P. R. Struck and G. Burkard, *Phys. Rev. B* **82**, 125401 (2010).
- [22] B. Muralidharan and S. Datta, *Phys. Rev. B* **76**, 035432 (2007).
- [23] A. Shandilya, S. Kapila, R. Krishnan, B. Weber, and B. Muralidharan, *ACS Applied Nano Materials* (2025), 10.1021/acsanm.5c01655.
- [24] A. V. Khaetskii and Y. V. Nazarov, *Phys. Rev. B* **64**, 125316 (2001).
- [25] V. N. Golovach, A. Khaetskii, and D. Loss, *Phys. Rev. Lett.* **93**, 016601 (2004).
- [26] L. Wang and G. Burkard, *Phys. Rev. B* **110**, 035409 (2024).
- [27] P. R. Struck and G. Burkard, *Phys. Rev. B* **82**, 125401 (2010).
- [28] M. Droth and G. Burkard, *Phys. Rev. B* **87**, 205432 (2013).
- [29] S. Abdelouahed, A. Ernst, J. Henk, I. Maznichenko, and I. Mertig, *Phys. Rev. B* **82**, 125424 (2010).
- [30] H. Min, J. Hill, N. A. Sinitsyn, B. Sahu, L. Kleinman, and A. H. MacDonald, *Phys. Rev. B* **74**, 165310 (2006).
- [31] P. Huang and X. Hu, *Phys. Rev. B* **89**, 195302 (2014).
- [32] P. Huang and X. Hu, *npj Quantum Inf.* **7**, 162 (2021).
- [33] A. Hosseinkhani and G. Burkard, *Phys. Rev. B* **104**, 085309 (2021).
- [34] W.-K. Tse and S. Das Sarma, *Phys. Rev. B* **79**, 235406 (2009).
- [35] J. Viljas and T. Heikkilä, *Phys. Rev. B* **81**, 245404 (2010).
- [36] K. Borysenko, J. Mullen, X. Li, Y. Semenov, J. Zavada, M. B. Nardelli, and K. Kim, *Phys. Rev. B* **83**, 161402 (2011).
- [37] T. Ando, *J. Phys. Soc. Jpn.* **74**, 777 (2005).
- [38] P. Huang and X. Hu, *Phys. Rev. B* **90**, 235315 (2014).
- [39] A. Hosseinkhani and G. Burkard, *Phys. Rev. B* **106**, 075415 (2022).
- [40] S. Braig and P. W. Brouwer, *Phys. Rev. B* **71**, 195324 (2005).
- [41] C. Timm, *Phys. Rev. B* **77**, 195416 (2008).
- [42] B. Muralidharan and M. Grifoni, *Phys. Rev. B* **88**, 045402 (2013).
- [43] F. Campaioli, J. H. Cole, and H. Hapuarachchi, *PRX Quantum* **5**, 020202 (2024).
- [44] M. S. Ferguson, D. Oehri, C. Rössler, T. Ihn, K. Ensslin, G. Blatter, and O. Zilberberg, *Phys. Rev. B* **96**, 235431 (2017).
- [45] D. Keith, S. Gorman, L. Kranz, Y. He, J. Keizer, M. Broome, and M. Simmons, *New J. Phys.* **21**, 063011 (2019).
- [46] R. Garreis, J. D. Gerber, V. Stará, C. Tong, C. Gold, M. Rössli, K. Watanabe, T. Taniguchi, K. Ensslin, T. Ihn, *et al.*, *Phys. Rev. Research* **5**, 013042 (2023).
- [47] P. Recher, J. Nilsson, G. Burkard, and B. Trauzettel, *Phys. Rev. B* **79**, 085407 (2009).

SUPPLEMENTARY MATERIAL

I. CALCULATION OF INTRINSIC RATES

Valley relaxation

Phonon noise: Dot eigenstates in valley $\tau \in \{K^+, K^-\}$ (with spin acting as a spectator) are described by two-component envelope functions [47]. The eigenstates take the form

$$\Psi_{nj}^{(\tau)}(r, \theta) = \frac{1}{\sqrt{2\pi}} \begin{pmatrix} F_{nj}(r)e^{i(j-1)\theta} \\ G_{nj}(r)e^{ij\theta} \end{pmatrix}, \quad (7)$$

with the normalization condition,

$$\int_0^\infty 2\pi r dr (|F_{nj}(r)|^2 + |G_{nj}(r)|^2) = 1.$$

The in-plane acoustic electron–phonon coupling (EPC) Hamiltonian in the bilayer graphene (BLG) sublattice basis can be written as [26, 37]

$$H_{\text{EPC}}^{\lambda q} = \frac{q}{\sqrt{A\rho\Omega_{\lambda q}}} [g_1 a_1(\lambda) + g_2 a_2(\lambda, \phi) \sigma_x] \left(e^{i\mathbf{q}\cdot\mathbf{r}} b_{\lambda q} - e^{-i\mathbf{q}\cdot\mathbf{r}} b_{\lambda q}^\dagger \right), \quad (8)$$

where $\Omega_{\lambda q} = v_\lambda q$ is the phonon frequency for branch λ , A is the sample area, and ρ is the mass density. The coefficients g_1 and g_2 correspond to the deformation potential (DP) and bond-length change (BLC) coupling mechanisms, respectively. The polarization factors satisfy $a_1 = i$ for longitudinal acoustic (LA) phonons and $a_1 = 0$ for transverse acoustic (TA) phonons, indicating that the DP couples only to LA phonons. The BLC coupling enters through $a_2(\lambda, \phi)$, with $a_2 = ie^{2i\phi}$ for LA modes and $a_2 = i$ for TA modes.

Acoustic phonons in BLG carry small momenta ($q \ll K$), and therefore direct intervalley scattering between the two valleys K^+ and K^- is strongly suppressed. As a result, the electron–phonon matrix elements are evaluated within a single valley basis, and the valley eigenstates are subsequently combined through the appropriate mixing coefficients. To evaluate the matrix elements, we expand the plane-wave factor as,

$$e^{i\mathbf{q}\cdot\mathbf{r}} = \sum_{m=-\infty}^{\infty} i^m J_m(qr) e^{im(\theta-\phi)}.$$

From this expansion the angular momentum selection rule follows directly

$$m = j' - j \equiv \Delta j.$$

At small phonon momenta the leading nonvanishing contribution corresponds to the dipole channel with $|\Delta j| = 1$. In this limit the Bessel function reduces to $J_{\pm 1}(qr) \simeq \frac{qr}{2}$.

The relevant radial overlap integrals then become

$$M_{n'n} = \int_0^\infty r^2 dr [F_{n'j\pm 1}(r) F_{nj}(r) + G_{n'j\pm 1}(r) G_{nj}(r)], \quad (9)$$

$$N_{n'n}^{AB} = \int_0^\infty r^2 dr [F_{n'j\pm 1}(r) G_{nj}(r) + G_{n'j\pm 1}(r) F_{nj}(r)]. \quad (10)$$

Here $M_{n'n}$ describes intra-sublattice processes associated with the DP coupling, while $N_{n'n}^{AB}$ corresponds to inter-sublattice transitions arising from BLC.

The corresponding matrix elements of the plane-wave operator are therefore

$$\langle n'j \pm 1 | e^{i\mathbf{q}\cdot\mathbf{r}} | nj \rangle_{\text{DP}} \simeq \pi q e^{\mp i\phi} M_{n'n},$$

$$\langle n'j \pm 1 | e^{i\mathbf{q}\cdot\mathbf{r}} | nj \rangle_{\text{BLC}} \simeq \pi q e^{\mp i\phi} N_{n'n}^{AB}.$$

Including the EPC prefactor $\frac{q}{\sqrt{A\rho\Omega_{\lambda q}}} = \frac{\sqrt{q}}{\sqrt{A\rho v_\lambda}}$, the one-phonon transition amplitudes become

$$A_{n'j\pm 1, nj}^{(\text{DP, LA})} = \frac{\sqrt{q}}{\sqrt{A\rho v_{\text{LA}}}} g_1 a_1(\text{LA}) (\pi q) e^{\mp i\phi} M_{n'n}, \quad (11)$$

$$A_{n'j\pm 1, nj}^{(\text{BLC, } \lambda)} = \frac{\sqrt{q}}{\sqrt{A\rho v_\lambda}} g_2 a_2(\lambda, \phi) (\pi q) e^{\mp i\phi} N_{n'n}^{AB}. \quad (12)$$

The phonon-induced relaxation rate is obtained from Fermi's golden rule (FGR)

$$\gamma_{n \rightarrow n'} = \frac{2\pi}{\hbar} \sum_{\lambda, q} \left| A_{n'n}^{(\lambda)} \right|^2 \delta(\Delta E - \hbar\omega_{\lambda q}). \quad (13)$$

For a two-dimensional (2D) phonon bath the momentum sum is replaced by $\sum_q \rightarrow A \int \frac{dq q}{2\pi}$.

Performing the density-of-states (DOS) integration yields a power-law dependence on the phonon momentum $\gamma \propto q^4$.

The valley splitting is determined by the valley Zeeman energy $\Delta E = g_v \mu_B B_\perp$, which fixes the phonon momentum through the energy conservation condition $q = \frac{\Delta E}{\hbar v_\lambda} \propto B_\perp$.

The valley relaxation rate therefore becomes,

$$\gamma_v(B_\perp) = \frac{g_1^2 |M_{n'n}|^2 + g_2^2 |N_{n'n}^{AB}|^2}{\rho v_\lambda^6 \hbar^5} (g_v \mu_B B_\perp)^4. \quad (14)$$

Thus the valley relaxation rate in BLG due to acoustic phonons follows the quartic magnetic-field scaling

$$\gamma_v(B_\perp) \propto (g_1^2 |M_{n'n}|^2 + g_2^2 |N_{n'n}^{AB}|^2) B_\perp^4, \quad (15)$$

which originates from the dipole-like selection rule $|\Delta j| = 1$ and the linear dispersion of acoustic phonons. Here the DP coupling g_1 contributes only through LA phonons, whereas the BLC coupling g_2 contributes to both LA and TA phonon branches.

Phonon noise: In addition to phonon-mediated processes, valley relaxation in BLG quantum dots (QD) can also be induced by fluctuating electric fields originating from Johnson noise in the surrounding circuit. These electric-field fluctuations couple to the electric dipole of the confined electron and provide an additional relaxation channel between valley states. The corresponding system–bath interaction Hamiltonian is,

$$H_{\text{int}}^J = -e \mathbf{r} \cdot \mathbf{E}(t), \quad (16)$$

where $\mathbf{E}(t)$ represents the electric field fluctuations arising from voltage noise in the surrounding circuit.

Using FGR, the transition rate between valley states can be written as,

$$\gamma_v^J = \frac{1}{\hbar^2} \int_{-\infty}^{\infty} d\tau e^{i\omega_v \tau} \langle E_\alpha(\tau) E_\alpha(0) \rangle |\langle n' | e r_\alpha | n \rangle|^2, \quad (17)$$

where $\omega_v = \Delta E/\hbar$ denotes the valley transition frequency and α labels the in-plane Cartesian components of the electric field.

The electric-field fluctuations are related to voltage fluctuations across the circuit impedance R . The spectral density of voltage noise is given by,

$$S_V(\omega) = 2R\hbar\omega \coth\left(\frac{\hbar\omega}{2k_B T}\right). \quad (18)$$

In the low-temperature limit ($\hbar\omega \gg k_B T$), the thermal factor approaches unity and the spectrum reduces to the quantum limit, $S_V(\omega) \simeq 2R\hbar\omega$.

The electric-field spectral density is related to the voltage noise through the characteristic dot–gate coupling length l ,

$$S_E(\omega) \simeq \frac{S_V(\omega)}{l^2} = \frac{2R\hbar\omega}{l^2}. \quad (19)$$

The electric field couples to the dipole moment associated with the valley degree of freedom. The dipole matrix element between valley eigenstates can therefore be written as, $|\langle n' | e \mathbf{r} | n \rangle|^2 = e^2 d_v^2$, where d_v denotes the effective valley dipole length arising from the spatial structure of the valley eigenstates. In electrostatically defined BLG QDs, the valley eigenstates are not perfectly orthogonal in real space due to the finite confinement potential and the presence of intervalley mixing. This generates a small but finite electric dipole moment d_v , which enables coupling between valley states and fluctuating electric fields.

Substituting these expressions into FGR yields,

$$\gamma_v^J(\omega_v) = \frac{1}{\hbar^2} S_E(\omega_v) e^2 d_v^2. \quad (20)$$

Using $\omega_v = g_v \mu_B B_\perp/\hbar$, the magnetic-field dependence of the relaxation rate becomes,

$$\gamma_v^J(B_\perp) = \frac{2R}{\hbar^2 l^2} e^2 d_v^2 (g_v \mu_B B_\perp). \quad (21)$$

Thus the Johnson-noise-mediated valley relaxation rate scales linearly with B_\perp , in contrast to the quartic magnetic-field dependence of the phonon-mediated valley relaxation derived above. The prefactor depends on the circuit resistance R , the electrostatic length scale l , and the effective valley dipole length d_v characterizing the coupling between the valley states and the fluctuating electric field.

Spin relaxation

Phonon noise: Spin relaxation in BLG QDs arises primarily through the admixture mechanism, in which spin-orbit coupling (SOC) mixes opposite-spin states within the orbital spectrum of the dot. A weak SOC Hamiltonian H_{SO} , admixes the spin state $|0, \uparrow\rangle$ with excited states (ES) $|n, \downarrow\rangle$. The strength of this admixture is quantified by

$$\eta_n = \frac{\langle n, \downarrow | H_{\text{SO}} | 0, \uparrow \rangle}{E_0 - E_n} \propto \Delta_R,$$

where Δ_R denotes the Rashba spin splitting.

Because the electron-phonon interaction conserves spin, a spin flip cannot occur through EPC alone. The leading contribution therefore arises from a second-order process involving both the SO interaction and the electron-phonon interaction. The corresponding transition amplitude can be written as

$$M_{\downarrow\uparrow}^{(\lambda q)} = \sum_{n \neq 0} \left[\frac{\langle 0, \downarrow | H_{\text{EPC}}^{\lambda q} | n, \downarrow \rangle \langle n, \downarrow | H_{\text{SO}} | 0, \uparrow \rangle}{E_0 - E_n} + \frac{\langle 0, \downarrow | H_{\text{SO}} | n, \uparrow \rangle \langle n, \uparrow | H_{\text{EPC}}^{\lambda q} | 0, \uparrow \rangle}{E_0 - E_n} \right]. \quad (22)$$

The energy splitting between the two spin states is determined by the spin Zeeman energy, $\Delta E = g_s \mu_B B_{\perp}$. The emitted acoustic phonon therefore satisfies $\hbar\omega = \Delta E$.

At low B_{\perp} the transition amplitude reduces to an admixture prefactor proportional to Δ_R multiplied by an orbital EPC matrix element. The angular dependence of the resulting transition probability is captured by

$$f(\theta) = \cos^4\left(\frac{\theta}{2}\right) + \sin^4\left(\frac{\theta}{2}\right) = \frac{3 + \cos(2\theta)}{4}, \quad (23)$$

which arises from the angular structure of the dipole matrix elements associated with the phonon propagation direction.

To evaluate the orbital matrix elements we expand the plane-wave factor for small phonon momenta,

$$e^{i\mathbf{q}\cdot\mathbf{r}} \simeq 1 + i\mathbf{q}\cdot\mathbf{r}.$$

Defining the dipole matrix elements by $\mathbf{r}_{n0} = \langle n | \mathbf{r} | 0 \rangle$, and using the angular momentum selection rule $\Delta j = \pm 1$, the EPC matrix elements take the form

$$\langle 0 | H_{\text{EPC}}^{\text{LA, DP}} | n \rangle \propto g_1 \frac{q}{\sqrt{\Omega_{\text{LA}q}}} (i\mathbf{q}\cdot\mathbf{r}_{n0}),$$

which leads to

$$|\langle 0 | H | n \rangle|^2 \propto g_1^2 \frac{q^4}{\Omega_{\text{LA}q}} = g_1^2 \frac{q^3}{v_{\text{LA}}}.$$

Similarly, for BLC coupling mechanisms, we obtain,

$$\langle 0 | H_{\text{EPC}}^{\text{BLC}} | n \rangle \propto g_2 \frac{1}{\sqrt{\Omega_{\lambda q}}} (i\mathbf{q}\cdot\mathbf{r}_{n0}),$$

which yields

$$|\langle 0 | H | n \rangle|^2 \propto g_2^2 \frac{q^2}{\Omega_{\lambda q}} = g_2^2 \frac{q}{v_{\lambda}}.$$

Applying FGR, the deformation-DP contribution to the spin relaxation rate becomes

$$\gamma_s^{\lambda, \text{DP}}(B_{\perp}) = \frac{C_{\text{DP}} g_1^2 (\Delta E)^4}{\rho v_{\text{LA}}^6} f(\theta) \left| \sum_{n' \neq n} M_{n'n} R_{n'n} (\delta_{j,j+1} N_{n'n}^{AB} + \delta_{j,j-1} N_{n'n}^{AB}) \right|^2, \quad (24)$$

where C_{DP} is a numerical prefactor and $M_{n'n}$ and $R_{n'n}$ denote orbital overlap integrals.

The BLC mechanism yields

$$\gamma_s^{\lambda, \text{BLC}}(B_{\perp}) = \frac{C_{\text{BLC}}^{\lambda} g_2^2 (\Delta E)^2}{\rho v_{\lambda}^4} f(\theta) \left| \sum_{n' \neq n} R_{n'n} [\delta_{j,j+1} (N_{n'n}^{AB})^2 + \delta_{j,j-1} (N_{n'n}^{AB})^2] \right|^2. \quad (25)$$

These power-law scalings arise from the combined effect of the SOC-induced admixture amplitude, the dipole-like orbital matrix element, and the linear dispersion of in-plane acoustic phonons.

In contrast, direct spin–phonon coupling to out-of-plane flexural (ZA) phonons, which can arise in graphene through curvature-induced spin–orbit interactions, is not operative in the hBN-encapsulated device geometry considered here. In electrostatically defined BLG QDs within such gate stacks, flexural distortions are strongly suppressed, and the dominant spin relaxation channels therefore originate from the in-plane acoustic phonon mechanisms derived above.

Johnson noise: In addition to phonon-mediated processes, fluctuating electric fields generated by Johnson noise in the surrounding circuit provide an additional relaxation channel. These electric-field fluctuations couple to the dipole moment induced by SOC admixture and can drive spin transitions. The corresponding relaxation rate can be written as

$$\gamma_s^J(B_{\perp}) = \frac{2R}{\hbar^2 l^2} e^2 d_s^2 \Delta E, \quad (26)$$

where R is the effective circuit resistance, l denotes the dot–gate distance, and d_s is the effective dipole length associated with the SOC-induced spin admixture. Using $\Delta E = g_s \mu_B B_{\perp}$, this becomes

$$\gamma_s^J(B_{\perp}) = \frac{2R}{\hbar^2 l^2} e^2 d_s^2 (g_s \mu_B B_{\perp}). \quad (27)$$

Thus the Johnson-noise-mediated spin relaxation rate scales linearly with the B_{\perp} .

Absence of Van Vleck cancellation for spin and valley qubits in BLG: The leading-order spin–phonon matrix elements do not cancel at zero magnetic field because the two spin states involved in the transition are not related by time reversal. Consequently, the Van Vleck cancellation that suppresses relaxation between Kramers partners is absent for both valley and spin mediated transitions and the relaxation rates retain the lowest-order B_{\perp} scaling derived above.

Kramers relaxation

Phonon noise: Kramers partners within a single dot orbital n are related by time reversal \mathcal{T} ,

$$|i\rangle = |n, K^+, \uparrow_B\rangle, \quad |f\rangle = \mathcal{T}|i\rangle = |n, K^-, \downarrow_B\rangle.$$

The H_{EPC} is time-reversal even, while the spin–orbit interaction H_{SO} admixes opposite-spin virtual states. The lowest nonzero one-phonon process is therefore second order, involving one EPC vertex and one SOC vertex. The corresponding effective transition amplitude is

$$M_{\text{eff}}(\mathbf{q}) = \sum_m \frac{\langle f | H_{\text{EPC}} | m \rangle \langle m | H_{\text{SO}} | i \rangle}{E_i - E_m - \frac{1}{2} E_Z} + \sum_m \frac{\langle f | H_{\text{SO}} | m \rangle \langle m | H_{\text{EPC}} | i \rangle}{E_i - E_m + \frac{1}{2} E_Z},$$

where $E_Z = g_s \mu_B B_{\perp}$ and the sum runs over orbital excitations $|m\rangle$ with the appropriate valley structure. Let $\Delta_m = (E_n - E_m)_{B_{\perp}=0}$. Expanding the denominators for small $E_Z = \hbar\omega$ gives,

$$\frac{1}{\Delta_m \mp E_Z/2} = \frac{1}{\Delta_m} \pm \frac{E_Z}{2} \frac{1}{\Delta_m^2} + O(E_Z^2).$$

Define the time-reversal-related matrix elements

$$A_m = \langle f | H_{\text{EPC}} | m \rangle \langle m | H_{\text{SO}} | i \rangle, \quad B_m = \langle f | H_{\text{SO}} | m \rangle \langle m | H_{\text{EPC}} | i \rangle.$$

For a Kramers pair and time-reversal-even H_{EPC} , one has $B_m = -A_m$ at $B_\perp = 0$. Consequently, the E_Z^0 term cancels exactly (Van Vleck cancellation), and the leading contribution is linear in E_Z ,

$$M_{\text{eff}}(\mathbf{q}) = \frac{E_Z}{2} \sum_m \frac{A_m - B_m}{\Delta_m^2} + O(E_Z^2) = E_Z \sum_m \frac{A_m}{\Delta_m^2} + O(E_Z^2) \propto \omega.$$

Thus, unlike the spin and valley channels, the effective Kramers transition amplitude acquires one explicit power of ω purely from Van Vleck cancellation.

For long-wavelength acoustic phonons, we use the dipole limit $e^{i\mathbf{q}\cdot\mathbf{r}} \simeq 1 + i\mathbf{q}\cdot\mathbf{r}$ between different orbitals, with the selection rule $\Delta j = \pm 1$. The EPC vertices may then be written as

$$V_{fm}^{(\lambda)} = \frac{q}{\sqrt{A\rho\Omega_{\lambda q}}} (\mathbf{q} \cdot \mathbf{d}_{0m}^{(\lambda)}), \quad \Omega_{\lambda q} = v_\lambda q,$$

where $\mathbf{d}_{0m}^{(\lambda)}$ denotes the dipole overlap for phonon branch λ . After angular averaging in two dimensions,

$$|\overline{\hat{\mathbf{q}} \cdot \mathbf{d}}|_\phi^2 = \frac{1}{2} |\mathbf{d}|^2.$$

We collect the phonon channels through the effective coupling constants

$$|g_\lambda|^2 = \begin{cases} g_1^2, & (\text{LA, DP}), \\ g_2^2, & (\text{LA, BLC}) \text{ or } (\text{TA, BLC}), \\ 0, & (\text{TA, DP}), \end{cases}$$

and define the radial dipole overlaps, consistent with $\Delta j = \pm 1$,

$$|d_{0m}^{(\text{DP})}|^2 \rightarrow |M_{m0}|^2, \quad M_{m0} = \int_0^\infty dr r^2 [F_m F_0 + G_m G_0],$$

$$|d_{0m}^{(\text{BLC})}|^2 \rightarrow |N_{m0}^{AB}|^2, \quad N_{m0}^{AB} = \int_0^\infty dr r^2 [F_m G_0 + G_m F_0].$$

Using Fermi's golden rule, the phonon-induced Kramers relaxation rate is

$$\gamma^{(\lambda)} = \frac{2\pi}{\hbar} \frac{A}{(2\pi)^2} \int d^2 q \delta(\hbar\Omega_{\lambda q} - \hbar\omega) \overline{|M_{\text{eff}}(\mathbf{q})|}_\phi^2.$$

Together with

$$\int q dq q^3 \delta(\hbar v_\lambda q - \hbar\omega) = \frac{q_0^4}{\hbar v_\lambda}, \quad q_0 = \frac{\omega}{v_\lambda},$$

and the linear-in- E_Z effective amplitude above, one obtains the characteristic B_\perp^6 scaling for Kramers relaxation,

$$\gamma_k^{(\lambda)} \propto \frac{\omega^6}{v_\lambda^6} \sum_m \frac{|\langle m | H_{\text{SO}} | i \rangle|^2}{\Delta_m^4} \times \begin{cases} g_1^2 |M_{m0}|^2, & (\text{LA, DP}), \\ g_2^2 |N_{m0}^{AB}|^2, & (\text{LA/TA, BLC}). \end{cases}$$

Restoring prefactors, the explicit rates read

$$\gamma_k^{(\text{LA,DP})} = \frac{g_1^2}{4\pi\rho} \frac{\omega^6}{v_{\text{LA}}^6} \sum_m \frac{|\langle m | H_{\text{SO}} | i \rangle|^2}{\Delta_m^4} |M_{m0}|^2, \quad (28)$$

$$\gamma_k^{(\text{LA,BLC})} = \frac{g_2^2}{4\pi\rho} \frac{\omega^6}{v_{\text{LA}}^6} \sum_m \frac{|\langle m | H_{\text{SO}} | i \rangle|^2}{\Delta_m^4} |N_{m0}^{AB}|^2, \quad (29)$$

$$\gamma_{\mathbf{k}}^{(\text{TA,BLC})} = \frac{g_2^2}{4\pi\rho} \frac{\omega^6}{v_{\text{TA}}^6} \sum_m \frac{|\langle m|H_{\text{SO}}|i\rangle|^2}{\Delta_m^4} |N_{m0}^{AB}|^2. \quad (30)$$

The TA mode has no contribution from the DP channel to linear order. Here, $\omega = \frac{E_Z}{\hbar} = \frac{g_s\mu_B B_{\perp}}{\hbar}$. The Van Vleck cancellation at $B_{\perp} = 0$ eliminates the field-independent contribution to the transition amplitude. As a result, the leading term of the effective matrix element becomes proportional to the transition frequency ω . When this frequency dependence is combined with the dipole coupling to phonons and the phase space available to 2D acoustic phonons, the relaxation rate acquires a characteristic scaling proportional to B_{\perp}^6 for acoustic-phonon-induced relaxation between Kramers partners in BLG.

Johnson noise: In addition to phonon-mediated processes, fluctuating electric fields generated by Johnson noise in the surrounding circuit provide an additional relaxation channel for the Kramers qubit. The corresponding interaction Hamiltonian is

$$H_{\text{int}}^J = -e\mathbf{r} \cdot \mathbf{E}(t). \quad (31)$$

For the Kramers pair

$$|i\rangle = |n, K^+, \uparrow_B\rangle, \quad |f\rangle = \mathcal{T}|i\rangle = |n, K^-, \downarrow_B\rangle,$$

the direct dipole matrix element vanishes at $B_{\perp} = 0$ because H_{int}^J is time-reversal even. The leading nonzero contribution therefore arises through second-order admixture with virtual ES,

$$D_{\text{eff}}^{(\alpha)} = \sum_m \frac{\langle f|er_{\alpha}|m\rangle\langle m|H_{\text{SO}}|i\rangle}{E_i - E_m - \frac{1}{2}E_Z} + \sum_m \frac{\langle f|H_{\text{SO}}|m\rangle\langle m|er_{\alpha}|i\rangle}{E_i - E_m + \frac{1}{2}E_Z}, \quad (32)$$

where $E_Z = g_s\mu_B B_{\perp}$. Defining,

$$A_m^{(\alpha)} = \langle f|er_{\alpha}|m\rangle\langle m|H_{\text{SO}}|i\rangle, \quad B_m^{(\alpha)} = \langle f|H_{\text{SO}}|m\rangle\langle m|er_{\alpha}|i\rangle,$$

and $\Delta_m = (E_n - E_m)_{B_{\perp}=0}$, one has $B_m^{(\alpha)} = -A_m^{(\alpha)}$ at $B_{\perp} = 0$. Expanding for small E_Z then gives

$$D_{\text{eff}}^{(\alpha)} = E_Z \sum_m \frac{A_m^{(\alpha)}}{\Delta_m^2} + O(E_Z^2) \propto B_{\perp}.$$

Using Fermi's golden rule, the Johnson-noise-induced Kramers relaxation rate is

$$\gamma_{\mathbf{k}}^J = \frac{1}{\hbar^2} \sum_{\alpha} S_{E_{\alpha}}(\omega) \left| D_{\text{eff}}^{(\alpha)} \right|^2, \quad \omega = \frac{E_Z}{\hbar}. \quad (33)$$

In the low-temperature quantum Johnson-noise regime,

$$S_E(\omega) = \frac{2R\hbar\omega}{l^2},$$

so that,

$$\gamma_{\mathbf{k}}^J(B_{\perp}) = \frac{2R}{\hbar^3 l^2} (g_s\mu_B B_{\perp})^3 \sum_{\alpha} \left| \sum_m \frac{\langle f|er_{\alpha}|m\rangle\langle m|H_{\text{SO}}|i\rangle}{\Delta_m^2} \right|^2. \quad (34)$$

Thus the Johnson-noise-mediated Kramers relaxation rate follows the scaling, $\gamma_{\mathbf{k}}^J(B_{\perp}) \propto B_{\perp}^3$.

II. SPIN-VALLEY MIXING INDUCED BY INTERVALLEY COUPLING

In Sec. I we derived the intrinsic relaxation rates associated with transitions between the pure eigenstates of the BLG QD arising from electron-phonon and Johnson-noise coupling. Near spectral anticrossings, hybridization modifies the

eigenbasis, and the observable transition rates between the hybridized states become weighted combinations of these intrinsic rates.

We first consider the anticrossing arising from intervalley coupling, parametrized by the coupling strength t_v . In this regime the intervalley interaction mixes states belonging to the two valleys. The resulting eigenstates become superpositions of K^+ and K^- valley components. The relevant eigenstates close to the anticrossing can therefore be written as

$$\begin{aligned}
|1\rangle &= |K^-, \uparrow\rangle, \\
|\bar{2}\rangle &= \sin\left(\frac{\theta}{2}\right) |K^+, \downarrow\rangle - \cos\left(\frac{\theta}{2}\right) |K^-, \downarrow\rangle, \\
|\bar{3}\rangle &= \cos\left(\frac{\theta}{2}\right) |K^+, \downarrow\rangle + \sin\left(\frac{\theta}{2}\right) |K^-, \downarrow\rangle, \\
|4\rangle &= |K^+, \uparrow\rangle.
\end{aligned} \tag{35}$$

Here θ denotes the intervalley mixing angle determined by the competition between t_v and the detuning between the uncoupled spin–valley states. Far from the anticrossing the eigenstates approach pure valley states, while near the anticrossing they become strongly hybridized.

Because the hybridized states contain contributions from multiple spin–valley configurations, transitions between them receive contributions from several intrinsic relaxation channels simultaneously. The intrinsic rates derived in Sec. I correspond to

- γ_s : spin flip within the same valley,
- γ_v : valley flip without spin flip,
- γ_k : combined spin–valley (Kramers) transition.

These intrinsic processes combine to produce the effective relaxation rates between the hybridized eigenstates.

(i) *Transition $\bar{2} \rightarrow 1$.* We evaluate

$$\gamma_{\bar{2}1} = |\langle 1 | H_{e\text{-ph}} | \bar{2} \rangle|^2.$$

Using

$$|\bar{2}\rangle = \sin\left(\frac{\theta}{2}\right) |K^+, \downarrow\rangle - \cos\left(\frac{\theta}{2}\right) |K^-, \downarrow\rangle,$$

the matrix element becomes

$$\begin{aligned}
\langle 1 | H_{e\text{-ph}} | \bar{2} \rangle &= \sin\left(\frac{\theta}{2}\right) \langle K^-, \uparrow | H_{e\text{-ph}} | K^+, \downarrow \rangle \\
&\quad - \cos\left(\frac{\theta}{2}\right) \langle K^-, \uparrow | H_{e\text{-ph}} | K^-, \downarrow \rangle \\
&= \sin\left(\frac{\theta}{2}\right) M_k - \cos\left(\frac{\theta}{2}\right) M_s.
\end{aligned}$$

The corresponding relaxation rates follow from FRG, $\gamma = \frac{2\pi}{\hbar} \sum_{\mathbf{q}, \lambda} |M|^2 \delta(E_i - E_f - \hbar\omega_{\mathbf{q}\lambda})$, where $M = \langle f | H_{e\text{-ph}} | i \rangle$ denotes the relevant electron–phonon matrix element. Accordingly, the intrinsic relaxation channels satisfy

$$\begin{aligned}
\gamma_s &\propto |M_s|^2, \\
\gamma_k &\propto |M_k|^2, \\
\gamma_v &\propto |M_v|^2.
\end{aligned}$$

Squaring the matrix element gives

$$\begin{aligned}
|\langle 1 | H_{e\text{-ph}} | \bar{2} \rangle|^2 &= \left| \sin\left(\frac{\theta}{2}\right) M_k - \cos\left(\frac{\theta}{2}\right) M_s \right|^2 \\
&= \sin^2\left(\frac{\theta}{2}\right) |M_k|^2 + \cos^2\left(\frac{\theta}{2}\right) |M_s|^2 \\
&\quad - 2 \sin\left(\frac{\theta}{2}\right) \cos\left(\frac{\theta}{2}\right) \text{Re}(M_k M_s^*).
\end{aligned}$$

Assuming orthogonality of the phonon-induced matrix elements (no interference),

$$\gamma_{\bar{2}1} = \gamma_s \cos^2\left(\frac{\theta}{2}\right) + \gamma_k \sin^2\left(\frac{\theta}{2}\right). \tag{36}$$

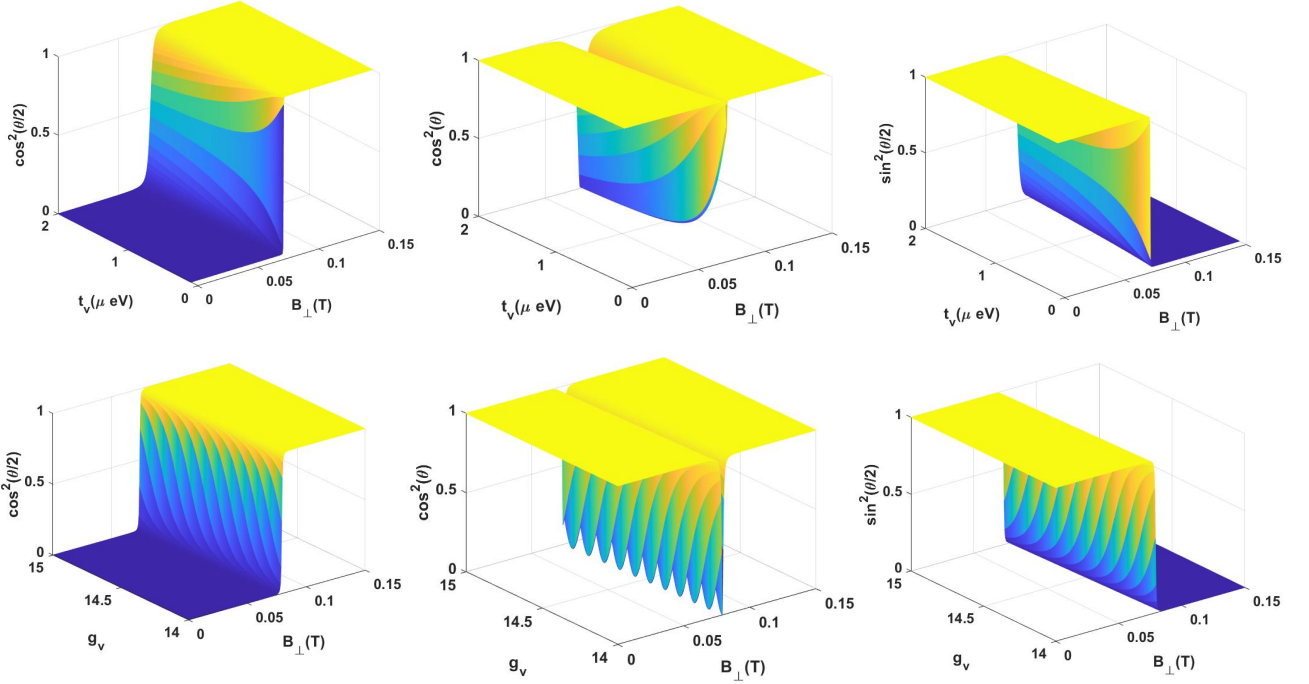


FIGURE 6. Magnetic-field dependence of the state-mixing coefficients near the spin-valley anticrossing. At low and high B_{\perp} , the eigenstates remain nearly pure spin or valley, while near the anticrossing they strongly hybridize. The upper panels show the evolution of $\cos^2(\theta/2)$ and $\sin^2(\theta/2)$ as functions of intervalley coupling t_v and perpendicular field B_{\perp} , while the lower panels illustrate the corresponding dependence on the valley g_v . The results highlight that both t_v and g_v critically tune the degree of hybridization at the anticrossing.

(ii) *Transition $\bar{3} \rightarrow 1$.* We evaluate

$$\gamma_{\bar{3}1} = |\langle 1 | H_{e-ph} | \bar{3} \rangle|^2.$$

Using

$$|\bar{3}\rangle = \cos\left(\frac{\theta}{2}\right) |K^+, \downarrow\rangle + \sin\left(\frac{\theta}{2}\right) |K^-, \downarrow\rangle,$$

we obtain

$$\langle 1 | H_{e-ph} | \bar{3} \rangle = \cos\left(\frac{\theta}{2}\right) M_k + \sin\left(\frac{\theta}{2}\right) M_s.$$

Squaring and neglecting interference terms gives

$$\gamma_{\bar{3}1} = \gamma_s \sin^2\left(\frac{\theta}{2}\right) + \gamma_k \cos^2\left(\frac{\theta}{2}\right). \quad (37)$$

(iii) *Transition $\bar{3} \rightarrow \bar{2}$.* This corresponds to a valley-flip transition between mixed down-spin states. Only matrix elements of the form

$$\langle K^+, \downarrow | H_{e-ph} | K^-, \downarrow \rangle = M_v$$

contribute. Expanding the hybridized states gives

$$\begin{aligned} \langle \bar{2} | H_{e-ph} | \bar{3} \rangle &= \sin\left(\frac{\theta}{2}\right) \cos\left(\frac{\theta}{2}\right) \left(\langle K^+, \downarrow | H_{e-ph} | K^-, \downarrow \rangle \right. \\ &\quad \left. - \langle K^-, \downarrow | H_{e-ph} | K^+, \downarrow \rangle \right). \end{aligned}$$

By symmetry this reduces to the valley matrix element M_v , giving

$$\gamma_{\bar{3}\bar{2}} = \gamma_v \cos^2(\theta). \quad (38)$$

(iv) *Transitions* $4 \rightarrow \bar{3}$ and $4 \rightarrow \bar{2}$. These correspond to spin-flip processes from $|4\rangle = |K^+, \uparrow\rangle$ to the mixed down-spin states. The resulting rates are

$$\gamma_{4\bar{3}} = \gamma_s \cos^2\left(\frac{\theta}{2}\right) + \gamma_k \sin^2\left(\frac{\theta}{2}\right), \quad (39)$$

$$\gamma_{4\bar{2}} = \gamma_s \sin^2\left(\frac{\theta}{2}\right) + \gamma_k \cos^2\left(\frac{\theta}{2}\right). \quad (40)$$

(v) *Transition* $4 \rightarrow 1$. Finally, the transition between spin-up states in opposite valleys corresponds to a pure valley flip,

$$\gamma_{41} = \gamma_v. \quad (41)$$

Thus, intervalley hybridization redistributes the intrinsic relaxation channels derived in Sec. I, producing transition rates between hybridized states that depend explicitly on the mixing angle θ , defined through $\cos^2\left(\frac{\theta}{2}\right) = \frac{\sqrt{(\Delta_{SO} - E_Z)^2 + 4t_v^2} - (\Delta_{SO} - E_Z)}{2\sqrt{(\Delta_{SO} - E_Z)^2 + 4t_v^2}}$.

III. INTRA-VALLEY SPIN MIXING

We now consider the anticrossing that appears at higher magnetic fields in the BLG spectrum, arising from spin mixing within a single valley. In contrast to the previous case, this anticrossing does not originate from intervalley coupling but instead arises from spin mixing within a single valley. Spin-orbit coupling generates an effective intra-valley spin-flip matrix element t_s that hybridizes the states $|K^+, \uparrow\rangle$ and $|K^+, \downarrow\rangle$. Restricting to the K^+ subspace, the effective Hamiltonian can be written as

$$H_{K^+} = \frac{1}{2} \begin{pmatrix} \Delta_{SO} - E_Z & t_s \\ t_s & -(\Delta_{SO} - E_Z) \end{pmatrix}, \quad (42)$$

where $E_Z = g_s \mu_B B_\perp$ is the Zeeman energy. Diagonalizing this Hamiltonian yields the hybridized eigenstates given below,

$$|1\rangle = |K^-, \uparrow\rangle, \quad (43)$$

$$|2\rangle = |K^-, \downarrow\rangle, \quad (44)$$

$$|\bar{3}\rangle = \sin\left(\frac{\phi}{2}\right) |K^+, \uparrow\rangle - \cos\left(\frac{\phi}{2}\right) |K^+, \downarrow\rangle, \quad (45)$$

$$|\bar{4}\rangle = \cos\left(\frac{\phi}{2}\right) |K^+, \uparrow\rangle + \sin\left(\frac{\phi}{2}\right) |K^+, \downarrow\rangle. \quad (46)$$

The mixing angle ϕ is determined by the detuning between the spin-orbit splitting Δ_{SO} and the Zeeman energy E_Z , together with the intra-valley spin-flip matrix element t_s . Explicitly,

$$\cos^2\left(\frac{\phi}{2}\right) = \frac{\sqrt{(\Delta_{SO} - E_Z)^2 + 4t_s^2} + (\Delta_{SO} - E_Z)}{2\sqrt{(\Delta_{SO} - E_Z)^2 + 4t_s^2}}, \quad (47)$$

$$\sin^2\left(\frac{\phi}{2}\right) = \frac{\sqrt{(\Delta_{SO} - E_Z)^2 + 4t_s^2} - (\Delta_{SO} - E_Z)}{2\sqrt{(\Delta_{SO} - E_Z)^2 + 4t_s^2}}. \quad (48)$$

Because the eigenstates are now spin-mixed within a single valley, the intrinsic relaxation channels derived in Sec. I again combine to produce modified decay rates between the hybridized states.

Applying FGR yields

$$\begin{aligned}
\gamma_{21} &= \gamma_s, \\
\gamma_{\bar{3}1} &= \sin^2\left(\frac{\phi}{2}\right) \gamma_v + \cos^2\left(\frac{\phi}{2}\right) \gamma_k, \\
\gamma_{\bar{4}1} &= \cos^2\left(\frac{\phi}{2}\right) \gamma_v + \sin^2\left(\frac{\phi}{2}\right) \gamma_k, \\
\gamma_{\bar{3}2} &= \sin^2\left(\frac{\phi}{2}\right) \gamma_k + \cos^2\left(\frac{\phi}{2}\right) \gamma_v, \\
\gamma_{\bar{4}2} &= \cos^2\left(\frac{\phi}{2}\right) \gamma_k + \sin^2\left(\frac{\phi}{2}\right) \gamma_v, \\
\gamma_{\bar{4}\bar{3}} &= \sin^2 \phi \gamma_s.
\end{aligned} \tag{49}$$

The transition γ_{21} corresponds to a pure spin flip in the K^- valley and is therefore insensitive to the hybridization. The transitions $\gamma_{\bar{3}1}$ and $\gamma_{\bar{4}1}$ describe relaxation from the K^- states to the hybridized K^+ states, with the relative contributions of valley-conserving and spin-assisted processes controlled by the mixing angle ϕ .

Finally, the transition between the two hybridized K^+ states,

$$\gamma_{\bar{4}\bar{3}} = \sin^2 \phi \gamma_s,$$

represents intra-valley relaxation driven by spin mixing within the same valley. This process becomes significant only near the anticrossing where the hybridization is strongest, while far from the anticrossing the states revert to nearly pure spin eigenstates and the transition becomes strongly suppressed.

IV. MASTER-EQUATION (ME) DESCRIPTION OF THE LOAD-WAIT DYNAMICS

We consider a BLG QD operating in the Coulomb-blockade (CB) regime and coupled to a single electronic reservoir. In the load/wait stage of the experimental cycle the tunnel barrier to the reservoir is closed, suppressing charge exchange with the lead. The remaining dynamics are governed by intrinsic noise-induced relaxation processes between well-separated energy eigenstates of the dot. Because these processes occur incoherently and rapidly destroy phase coherence between eigenstates, off-diagonal density-matrix elements can be neglected. The dynamics therefore reduce to classical population evolution, allowing the system to be described by a Pauli master equation for the state probabilities rather than a full quantum master equation.

The relevant Hilbert space consists of the empty-dot state $|0\rangle$ and the four single-electron eigenstates $|i\rangle$ with energies E_i ($i = 1, \bar{2}, \bar{3}, 4$). The probability vector describing the system is [40–42],

$$\mathbf{P}(t) = (P_0(t), P_1(t), P_{\bar{2}}(t), P_{\bar{3}}(t), P_4(t))^T, \quad \sum_{i=0,1,\bar{2},\bar{3},4} P_i(t) = 1. \tag{50}$$

During the load/wait stage of the experimental cycle the tunnel barrier to the reservoir is closed, so that no tunneling processes occur between the dot and the contact. The electron number in the dot therefore remains fixed, and the dynamics are governed entirely by intrinsic relaxation processes within the QD. These processes originate from the phonon and Johnson-noise mechanisms derived in Sec. I.

Downhill transitions between dot levels are denoted by γ_{ij} for processes $i \rightarrow j$ when $E_i > E_j$. The corresponding uphill transitions arise from thermally activated phonon re-excitation and obey detailed balance,

$$\gamma_{ji} = \gamma_{ij} e^{-(E_i - E_j)/k_B T_e}, \quad (E_i > E_j),$$

where T_e is the electron temperature.

Because tunneling to the reservoir is suppressed in this regime, the empty-dot state remains unoccupied and

$$P_0(t) \equiv 0.$$

The dynamics therefore reduce to the four-state single-electron subspace

$$\mathbf{P}_{dot}(t) = (P_1(t), P_{\bar{2}}(t), P_{\bar{3}}(t), P_4(t))^T.$$

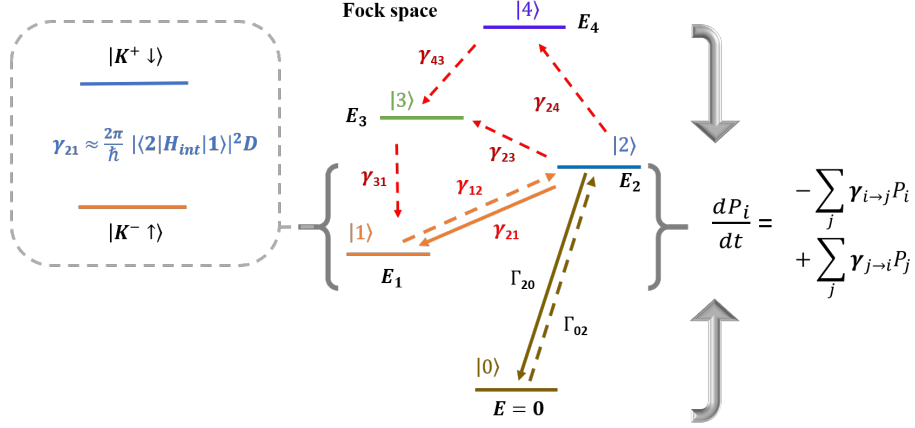


FIGURE 7. Multilevel transition network used in the ME model. The BLG QD is described by the empty state $|0\rangle$ and four single-electron states $|1\rangle$ – $|4\rangle$. Intrinsic relaxation processes between dot levels are characterized by rates γ_{ij} , while tunneling between the reservoir and the dot occurs with rates Γ_{0i} and Γ_{i0} . The populations evolve according to the Pauli ME. Near spectral anticrossings the eigenstates hybridize, leading to modified transition rates that enter the rate matrix.

The evolution of the populations is governed by the Pauli master equation

$$\dot{\mathbf{P}}_{dot}(t) = W_{dot} \mathbf{P}_{dot}(t), \quad (51)$$

where W_{dot} is the intra-dot transition matrix constructed from the intrinsic relaxation rates,

$$W_{dot} = \begin{pmatrix} -(\gamma_{12} + \gamma_{13} + \gamma_{14}) & \gamma_{21} & \gamma_{31} & \gamma_{41} \\ \gamma_{12} & -(\gamma_{21} + \gamma_{23} + \gamma_{24}) & \gamma_{32} & \gamma_{42} \\ \gamma_{13} & \gamma_{23} & -(\gamma_{31} + \gamma_{32} + \gamma_{34}) & \gamma_{43} \\ \gamma_{14} & \gamma_{24} & \gamma_{34} & -(\gamma_{41} + \gamma_{42} + \gamma_{43}) \end{pmatrix}. \quad (52)$$

The structure of W_{dot} ensures probability conservation, since the columns sum to zero. Consequently, the matrix possesses one eigenvalue equal to zero, corresponding to the stationary state. The remaining three eigenvalues $\{\lambda_1, \lambda_2, \lambda_3\}$ describe the relaxation modes of the coupled four-level system.

The general solution of the master equation can therefore be written as

$$P_i(t) = P_i^{(\infty)} + \sum_{j=1}^4 c_{ij} e^{-\lambda_j t}, \quad i = 1, \bar{2}, \bar{3}, 4, \quad (53)$$

where $P_i^{(\infty)}$ are the stationary probabilities. Since the system relaxes thermally within the dot subspace, the stationary distribution is given by the Boltzmann weights

$$P_i^{(\infty)} = \frac{e^{-E_i/k_B T_e}}{\sum_{m=1}^4 e^{-E_m/k_B T_e}}, \quad P_0^{(\infty)} = 0.$$

The coefficients c_{ij} are determined by the initial condition set during the load stage. For example, if the electron is initialized in state $\bar{2}$, the initial populations are

$$P_1(0) = 0, \quad P_{\bar{2}}(0) = 1, \quad P_{\bar{3}}(0) = 0, \quad P_4(0) = 0.$$

If phonon re-excitation processes were neglected, the decay of the ES $\bar{2}$ would be governed by the bare escape rate,

$$\gamma_{\bar{2}}^{\text{bare}} = \gamma_{21} + \gamma_{23} + \gamma_{24}.$$

This expression represents the total intrinsic transition probability out of state $\bar{2}$ in the absence of repopulation from other levels.

However, near the spectral anticrossing the ES $\bar{2}$ and $\bar{3}$ become closely spaced in energy. As B_{\perp} approaches the anticrossing point, the energy separation $E_{\bar{3}} - E_{\bar{2}}$ can become comparable to the thermal energy $k_B T_e$. In this regime thermally activated transitions between the two ESs become significant, allowing population to be transferred from $\bar{2}$ to $\bar{3}$ and vice versa.

Consequently, the decay dynamics can no longer be described as the relaxation of a single isolated level. Instead, the ES population evolves through the coupled dynamics of the nearly degenerate states $\bar{2}$ and $\bar{3}$, together with their relaxation pathways to lower-energy states. The time evolution of the ES occupation therefore becomes multi-exponential,

$$P_{\bar{2}}(t) = P_{\bar{2}}^{(\infty)} + \sum_{j=1}^3 A_j e^{-\lambda_j t},$$

where λ_j are the non-zero eigenvalues of the full rate matrix describing the coupled four-level system.

In this regime the experimentally observed decay rate is determined by the slowest relaxation mode of the rate matrix rather than by the escape rate of any individual transition channel. The effective relaxation rate is therefore

$$\gamma_{\text{effective}}(B_{\perp}) = \min\{\lambda_1, \lambda_2, \lambda_3\},$$

which corresponds to the smallest non-zero eigenvalue of the intra-dot transition matrix.

Importantly, $\gamma_{\text{effective}}$ is not associated with relaxation between any particular pair of states and cannot be obtained from a simple combination of the microscopic transition rates γ_{ij} . Instead it emerges from the collective dynamics of the coupled multilevel system, where population can repeatedly redistribute between the nearly degenerate ES before relaxing to the GS.

Near the state anticrossings, the proximity of higher excited states enables thermally activated population exchange, causing the observed lifetime to reflect the slowest relaxation mode of the coupled multilevel system. Consequently, although the qubit transitions remain spectroscopically well resolved, the lifetime extracted from the measurements (T_{1m}) at these operating points corresponds to this effective decay rate rather than to the intrinsic T_1 lifetime.

In the numerical simulations presented in the main text, the B_{\perp} -dependent intrinsic rates γ_{ij} derived in Secs. I–III are used to construct the rate matrix $W_{\text{dot}}(B_{\perp})$. Solving the ME yields the population dynamics and the corresponding γ_{eff} . Near the anticrossing, the proximity of ES modifies the decay dynamics: rather than a single exponential relaxation to zero population, the excited-state occupation approaches its Boltzmann value on a timescale determined by the smallest non-zero eigenvalue of the rate matrix.